Nano Today (2009) 4, 347—358

available at www.sciencedirect.com

ScienceDirect

journal homepage: www.elsevier.com/locate/nanotoday

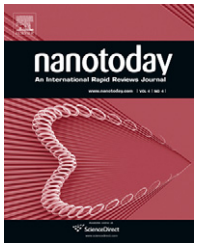

REVIEW

Advances in the synthesis of InAs and GaAs nanowires for electronic applications

Shadi A. Dayeh [1], Cesare Soci, Xin-Yu Bao [2], Deli Wang*

Department of Electrical and Computer Engineering, University of California-San Diego, 9500 Gilman Drive, La Jolla, CA 92093-0407, USA

Received 10 June 2009; received in revised form 17 June 2009; accepted 18 June 2009
Available online 5 July 2009

KEYWORDS
Nanowire;
III—V;
Electronics;
Optoelectronics

Summary New materials and device concepts are in great demand for continual (opto)electronic device scaling and performance enhancement. Arsenide III-V semiconductor nanowires promise novel device architectures and superior (opto)electronic properties. Recent insights into the growth and optimal control over the InAs and GaAs nanowire morphology and distinguished key physical aspects in their growth are discussed. Direct correlation of individual nanowire crystal structure with their electronic transport properties is also presented.
© 2009 Elsevier Ltd. All rights reserved.

Semiconductor device miniaturization enables high integration density, versatile functionality, and enhanced performance. With the current combination of materials and device architectures, further device scaling with improved performance is restricted by several fundamental limits. For example, technology node feature size of 65 nm in 2007 is projected to be 13 nm by 2022 [1], a goal that may not be achieved with the current high-k/Si technology. New materials with controlled morphologies and desired properties are being actively researched and assessed to meet future technological needs [2]. On the other hand, bottom-up fabrication of nanostructured materials is an appealing strategy that may provide alternative, unconventional methods to accomplish the miniaturization needs. Among these materials, semiconductor nanowires (NWs) have attracted a lot of attention [3—6]. For (opto)electronic applications, one-dimensional semiconductor NWs enable efficient diameter control [7], novel axial [8—10] and radial [11] heterostructure growth, size [12] and alloy [13] bandgap engineering, and the consequent rational implementation of functional devices, such as surround-gate field-effect transistors (FETs) [4,14,15], light emitting diodes [16], photodetectors [17,18], and waveguides [6,19]. In addition to the outstanding properties offered by NW dimensionality, III—V NWs top the list of semiconductor NWs in device performance due to their exceptionally high electron mobility [20,21], and possibility of low lasing threshold [22].

NWs of virtually any semiconductor material can be grown using the Chemical Vapor Deposition (CVD) or Molecular Beam Epitaxy (MBE) techniques or their variations mainly by the vapor—liquid—solid (VLS) mechanism [23]. Although VLS is the most commonly accepted NW growth mechanism, other mechanisms such as vapor—solid—solid [24,25], vapor—solid [26], oxide-assisted

* Corresponding author.
E-mail address: dwang@ece.ucsd.edu (D. Wang).
[1] Currently at the Center of Integrated Nanotechnologies, Los Alamos National Laboratory, Los Alamos, NM 87545, USA.
[2] Currently at the Department of Electrical Engineering, Stanford University, Stanford, CA 94305, USA.

1748-0132/$ — see front matter © 2009 Elsevier Ltd. All rights reserved.
doi:10.1016/j.nantod.2009.06.010

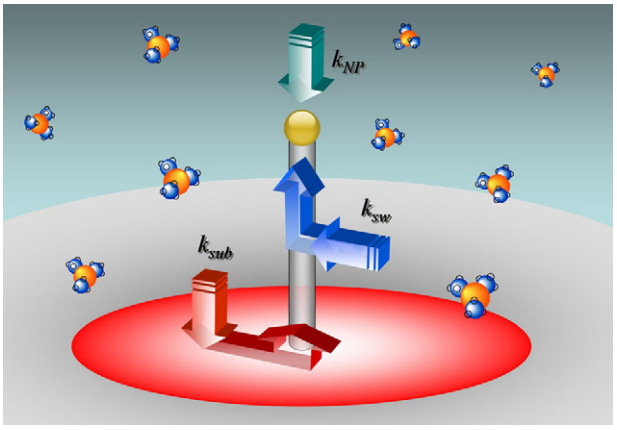

Figure 1 Illustration of NW VLS growth including group III flux impingement on the NP, NW sidewalls, and growth substrate, each contributing to the NW growth rate by k_{NP}, k_{sw}, and k_{sub}, respectively.

[27], solution—liquid—solution [28], and growth from thread dislocations [29,30] have also been proposed. The VLS NW growth is initiated and promoted by a metal nanoparticle (NP) catalyst: reactants in the vapor phase form a supersaturated liquid alloy inside the NP, precipitate at the liquid—solid interface and form the NW crystal. Material fluxes contributing to the growth may arise from direct impingement on the NP, NW sidewalls, or growth substrate leading to individual contribution to the NW growth rate dl/dt of k_{NP}, k_{sw}, and k_{sub}, respectively as illustrated in Fig. 1. Each of these contributions is proportional to the flux of reactant precursor impinging on the respective collection area, namely $S_{NW} = 2\pi r^2$ for material impinging on the NW top — considering 1/2 a sphere collection area — , $S_{sw} = 2\pi rl$ for material impinging on the NW sidewalls — considering a cylindrical collection area — , and $S_{sub} = \pi r_s^2$ for material impinging on the growth substrate — considering a circular collection area — , thus leading to a different growth rate behavior as we discuss below. Here, r is the *NW* radius, l is the *NW* length, and r_s is the radius of the collection area on the substrate for those adatoms that reach the *NW* tip and contribute to the VLS growth. This article summarizes recent understanding to the key effects of material impingement and diffusion in the III—V *NW* growth and morphology control, particularly for InAs and GaAs NWs, and provides direct correlation between their synthesis and resultant crystal structure with transport properties.

OMVPE growth of InAs and GaAs NWs

InAs and GaAs NWs can be synthesized using a variety of techniques including organo-metallic vapor phase epitaxy (OMVPE) [31], chemical [32] and molecular [33] beam epitaxy, chemical vapor deposition [34], laser ablation [35], and low-temperature solution techniques [36]. This section concerns with the OMVPE growth of Au-catalyzed InAs and GaAs NWs. Specifically, we discuss the temperature and precursor molar fraction effects on the NW morphology for both material systems and reveal through time-dependent growth studies that solid-phase diffusion of In adatoms is predominant in InAs NW growth whereas gas-phase diffusion of Ga species is predominant in GaAs NW growth. These results are also confirmed by the dependence of NW growth rate on the NP size. The InAs and GaAs NWs subject of this study were grown in an OMVPE reactor at 100 Torr chamber pressure utilizing arsine (AsH_3) and tri-methyl-indium (TMIn)/tri-methyl-gallium (TMGa) precursors, respectively, in H_2 carrier gas. For InAs NWs, an InAs (1 1 1)B or a SiO_2 substrate with Au NPs atop is heated to the desired growth temperature in AsH_3 flow. TMIn flow is only allowed to the reactor to grow the NWs for a specific growth time, after which the sample is cooled down to room temperature in AsH_3 flow. The same growth sequence is followed for GaAs NWs on a GaAs (1 1 1)B or Si (1 1 1) substrate with Au nanoparticles atop; however, an additional substrate-nanoparticle annealing step above 600 °C prior to growth is performed for the growths on Si (1 1 1) substrates. Apparent difference in morphology and the optimal growth conditions for InAs and GaAs NWs were found, the most prominent of which are related to the growth temperatures and precursor molar fractions.

Optimal control over the NW morphology

For NW growth to proceed in the VLS manner described in Fig. 1, a number of conditions need to be satisfied. According to Wagner and Ellis [37], and Givargizov [38], the NP must form a liquid solution with the material to be grown and must have a large contact angle (95—120°) with the growth substrate to enable its rise above the substrate. The chemical reactions should be possible but not favored kinetically so that the catalytic and adsorption properties of the liquid NP become effective in precursor decomposition and incorporation and consequently in the one-dimensional NW growth [39]. In addition, supersaturations in the NP are required especially in the initial stages of growth to enable NP rise above the substrate surface [38]. For vertical NW growth with respect to the substrate surface, the surface must also be oxide free. Since (1 1 1)A group-III terminated substrates are more easily oxidized than (1 1 1)B group-V terminated substrates, (1 1 1)B surfaces are usually preferred for NW growth. In addition, NP seeds tend to have larger contact angles on (1 1 1)A surfaces which cause instabilities in nucleation that increases non-vertical NW growth [40]. These requirements determine the temperature ranges over which NW growth can occur, which are typically 100—200 °C lower than those used for thin film growth. Low temperatures may not allow the formation of the liquid NP alloy and oxide desorption, whereas high temperatures increase the material solubility in the liquid NP and reduce its supersaturation and consequently the NW nucleation and growth rates. Within the growth temperature window, NW morphology may change depending primarily upon the growth temperature and the metal-organic molar fractions, to which we devote the rest of the discussion in this section.

We first consider the case of InAs NW morphology as function of both the growth temperature [41,42] and the precursor molar fractions [43]. At a fixed input molar V/III ratio of 60 and for a growth time of 6 min, the InAs NWs grown on InAs (1 1 1)B substrates are highly tapered at low growth temperatures of 450 and 475 °C and become more uniform as the temperature is increased up to 500 °C as

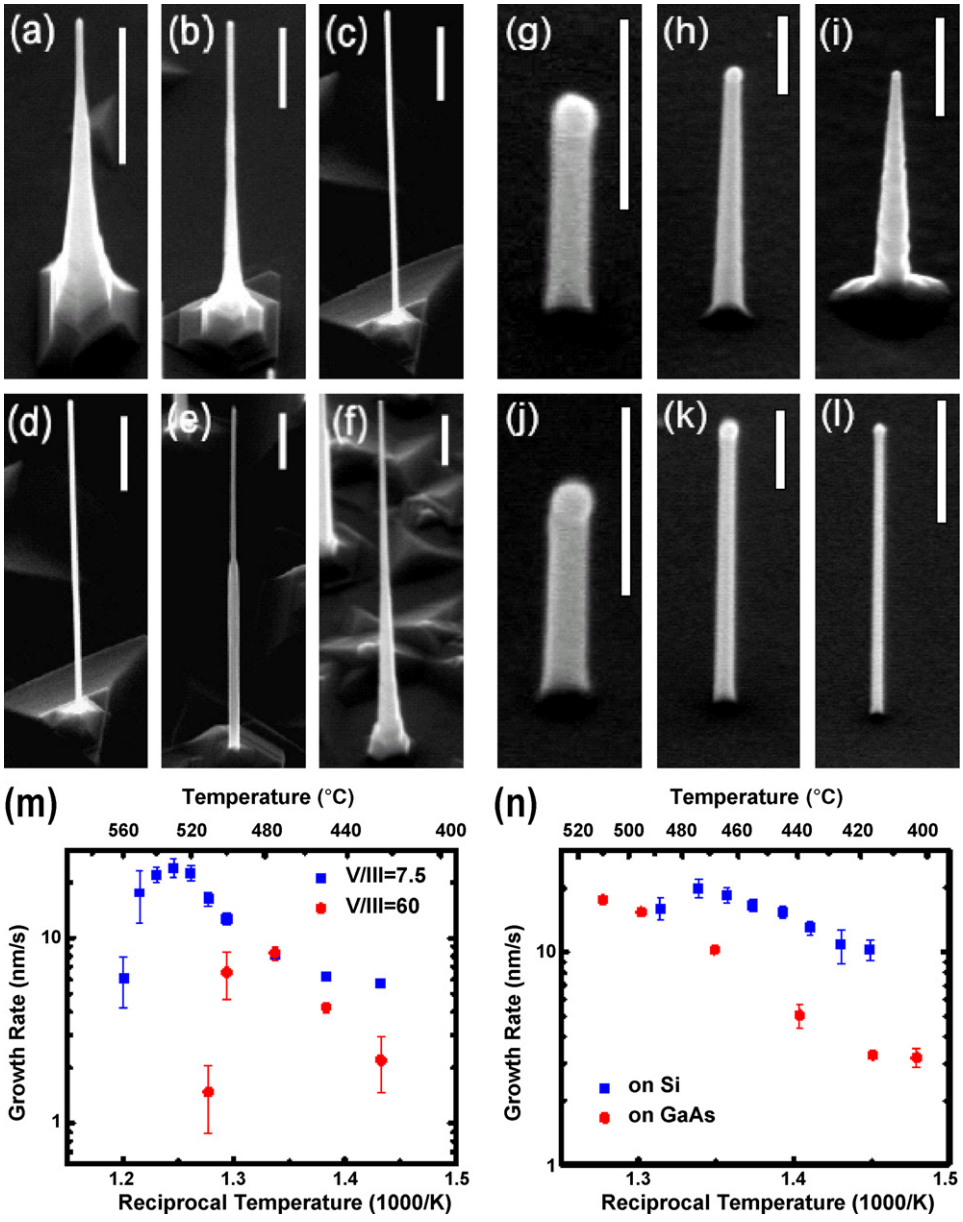

Figure 2 45° FE-SEM images of InAs NWs grown from 40 nm diameter Au NPs with a constant AsH_3 molar fraction of 8.32×10^{-4} at (a) 450 °C, (b) 475 °C, (c) 500 °C and constant TMIn molar fraction of 2.1×10^{-5}. InAs NWs grown at 500 °C and different TMIn molar fraction of (d) 2.1×10^{-5}, (e) 4.2×10^{-5}, and (f) 6.3×10^{-5}. Scale bars are 500 nm. 65° FE-SEM images of GaAs NWs grown from 50 nm diameter Au NPs with AsH_3 molar fraction of 7×10^{-4} and TMGa molar fraction of 1.1×10^{-4} at (g) 400 °C, (h) 470 °C, and (i) 510 °C. GaAs NWs grown at 412 °C with different TMGa molar fractions of (j) 1.1×10^{-4}, (k) 5.3×10^{-4}, and (l) 9×10^{-4} with constant V/III ratio of ~6.5. Scale bars are 200 nm for (g)–(k) and 500 nm for (l). (m) Temperature dependent growth rate of InAs NWs on InAs (1 1 1)B substrates for two different V/III ratios. Red dots are obtained at a TMIn molar fraction of 2.1×10^{-5} (V/III = 60) and blue squares were obtained at an input molar fraction of 1.7×10^{-4} (V/III = 7.5). (n) Temperature dependent growth rate of GaAs NWs on Si (1 1 1) (blue squares) and GaAs (1 1 1)B substrates (red dots). The red circles were obtained with AsH_3 molar fraction of 7×10^{-4} and TMGa molar fraction of 1.1×10^{-4}. The blue dots were obtained with AsH_3 molar fraction of 1.4×10^{-3} and TMGa molar fraction of 5.6×10^{-5} (V/III = 25). (Adapted with permission from Refs. [41,45,46]. ©2007 and 2008 American Chemical Society.)

illustrated in Fig. 2(a)–(c). The mobility of In adatoms that diffuse on the NW sidewalls to reach the molten Au–In NP increases at higher temperature, facilitating their incorporation at the NW tip rather than on the NW sidewalls. As the TMIn molar fraction increases at a constant temperature of 500 °C, the NW growth rate increases and substrate to NW diffusion of In adatoms prevails leading to NW tapering as illustrated in Fig. 2(d)–(f). Further increase in the TMIn molar fraction results in the formation of an In rich surface that allows growth of multiple InAs NWs per single Au nanoparticle [43,44].

The morphology dependence of GaAs NWs as function of temperature is opposite to that of InAs NWs where the GaAs NWs tend to be more tapered as the temperature

increases as shown in Fig. 2(g)–(i) due to enhanced surface growth on the GaAs NW sidewalls. Moreover, GaAs NW morphology is not sensitive to the TMGa molar fraction as demonstrated in Fig. 2 (j)–(m) [45]. This suggests a different diffusion/incorporation mechanism of Ga species on the NW sidewalls and NP surface as will be discussed later. With further increase of the TMGa molar fraction, ''worm-like'' surface growth in addition to NW growth is observed on the substrate [46]. This may be attributed to enhanced NP supersaturations leading to larger contact angles with the substrate and instabilities in NW nucleation.

The growth of InAs NWs ceases at high growth temperatures as has been previously observed [47]. We attributed this effect to an increase in the local/effective molar V/III ratio with temperature, which enhances thin film crystallization [48] and depletes necessary In concentration in the Au nanoparticle required for NW nucleation [41]. In other words, the supersaturation in the NP is reduced leading to nucleation deficiency. Thus, high TMIn flows are required to enable InAs NW growth at high temperatures. This is indeed the case where InAs NW growth, which was not possible at ~510 °C with a V/III ratio of 60, became possible with a V/III ratio of 7.5 up to ~550 °C as shown in Fig. 2(m), which shows Arrhenius plots of the InAs NW growth rate as function of temperature for two different V/III ratios. The InAs NW growth rate increases exponentially with temperature (prior to cessation), indicating kinetically limited growth with similar activation energy of ~116 kJ/mol for both V/III ratios used. This implies that the activation energy for NW elongation does not vary significantly with input V/III ratio once the InAs NW nucleates. Thin film growth rates, however, are dependent on the V/III ratio, which is attributed to differences in the probability of adsorption/desorption of adatoms on the substrate surface [49], and to the reduction of the pyrolysis activation energies as the input V/III ratio is increased [50]. GaAs NW growth on different surfaces [Si (1 1 1) and GaAs (1 1 1)B)] also increases exponentially with growth temperature as indicated in Fig. 2(n). The activation energies for GaAs NW growth was found to be ~57 kJ/mol on Si (1 1 1) surfaces and ~100 kJ/mol on GaAs (1 1 1)B surfaces [45]; the latter is similar to that of GaAs thin film growth [51]. This may be related to differences in precursor pyrolysis-temperatures on different surfaces and orientations [52]. Growth of GaAs NWs at high temperatures leads to enhanced thin film deposition at the growth substrate and NW sidewalls, which reduces the overall NW growth rates.

Species diffusion: solid-phase vs. gas-phase

Typically, growth of III–V NWs using OMVPE is considered to be diffusion-limited, i.e. growth rate increases for thinner diameter NWs [53] due to solid-phase diffusion over the substrate surface and NW sidewalls. During their investigation of the competitive or synergetic growth of GaP NWs, Borgström et al. have observed r dependent NW growth rates and proposed gas-phase diffusion of Ga species [54]. In addition, the Gibbs–Thomson effect (reduction of supersaturation for smaller r and therefore a drop in the NW growth rate) has been observed for GaAs NWs with small NP diameters and low V/III ratios [55]. Several models that take into account diffusion and Gibbs–Thomson effects have thus emerged [56–58]. Herein, we use both time and diameter dependent growth rates to distinguish between solid and gas-phase diffusion of group III species, which display distinct behavior in the growth of InAs and GaAs NWs.

The InAs NW growth from 40 nm diameter Au nanoparticles on InAs (1 1 1)B substrates at 500 °C was performed for different growth times. Fig. 3(a) and (b) shows FE-SEM images of InAs NWs grown with a TMIn molar fractions of 2.1×10^{-5} and 1.3×10^{-4}, respectively, as function of time [59]. Uniform NWs with 40 nm diameter dictating that of the Au nanoparticle are observed at the lower TMIn flow whereas tapered NWs with large diameters at their base are observed for the larger TMIn flow. Fig. 3(c) shows a plot of the InAs NW lengths as function of time for a relatively low TMIn molar fraction of 2.1×10^{-5}. The NW length increases exponentially at short growth time and becomes linear after about 3 min. This dependence can be attributed to the k_{sw} contribution to the growth rate depicted in Fig. 1, where $dl/dt \propto 2\pi rl$ results in exponential elongation of NWs due to the increase of collection area for In adatoms as the NW length increases. When the NW length exceeds the In adatom diffusion length on the NW surface ($l > \lambda_{NW}$), the collection area of In adatoms becomes constant ($dl/dt \propto 2\pi r\lambda_{NW}$), which results in linear NW elongation with time [60]. In the latter case, In adatoms that are one diffusion length away from the NW tip can either desorb or adsorb from or to the NW sidewalls leading to thickening of the NW diameter through a vapor–solid (VS) growth mechanism (Fig. 3(c)).

The transition from exponential to linear growth allows the extraction of the In diffusion length on the NW sidewalls [61] which was determined to be ~1 μm at 500 °C. This diffusion length is consistent with the length of the uniform portion near the tip of InAs NWs grown for longer growth time of 7 min as shown in inset of Fig. 3(c). In contrast, at higher TMIn molar fraction of 1.26×10^{-4}, the NW length varies sub-linearly with time for growth times shorter than 1.5 min, and then becomes linear, as depicted in Fig. 3(d). At high TMIn molar fraction, the nucleation time is shorter and the growth rate is higher than in the case of low TMIn molar fraction. The higher TMIn molar fraction allows longer In adatom diffusion on the (1 1 1)B substrate surface, thus increasing In adatom migration from the substrate to the NW sidewalls. This dependence can be attributed to the k_{sub} contribution to the total NW growth rate in Fig. 1, where $dl/dt \propto \pi r_s^2 = \pi(\lambda_{sub}/\lambda_{NW})^2(\lambda_{NW} - l)^2$, λ_{sub} being the In adatom diffusion length on the substrate surface. Here, an In adatom landing on the substrate surface and contributing to k_{sub} must travel a distance $\lambda_{eff} = r_s + l$ such that $\lambda_{eff} = \lambda_{NW}(l/\lambda_{NW}) + \lambda_{sub}(1 - l/\lambda_{NW})$ leading to $r_s = (\lambda_{sub}/\lambda_{NW})(\lambda_{NW} - l)$. This dependence of dl/dt on $(\lambda_{NW} - l)$ leads to the $\sim C\lambda_{NW}^2 t/(1 + C\lambda_{NW} t)$ time dependence observed for short NW length in Fig. 3(d), where C is a constant. At longer growth times, when $l > \lambda_{NW}$, the contribution from the substrate becomes irrelevant to NW elongation, and the NW length increases linearly with growth time due to the contributions of k_{sw} with $S_{sw} = 2\pi rl_{NW}$ similar to the case presented in Fig. 3(c).

This allows distinguishing between two NW growth regimes. In the first regime, where substrate to NW diffusion is minimal, the NW length increases exponentially with time and uniform NWs can be obtained for short growth times. In the second regime, where substrate-to-NW diffusion is

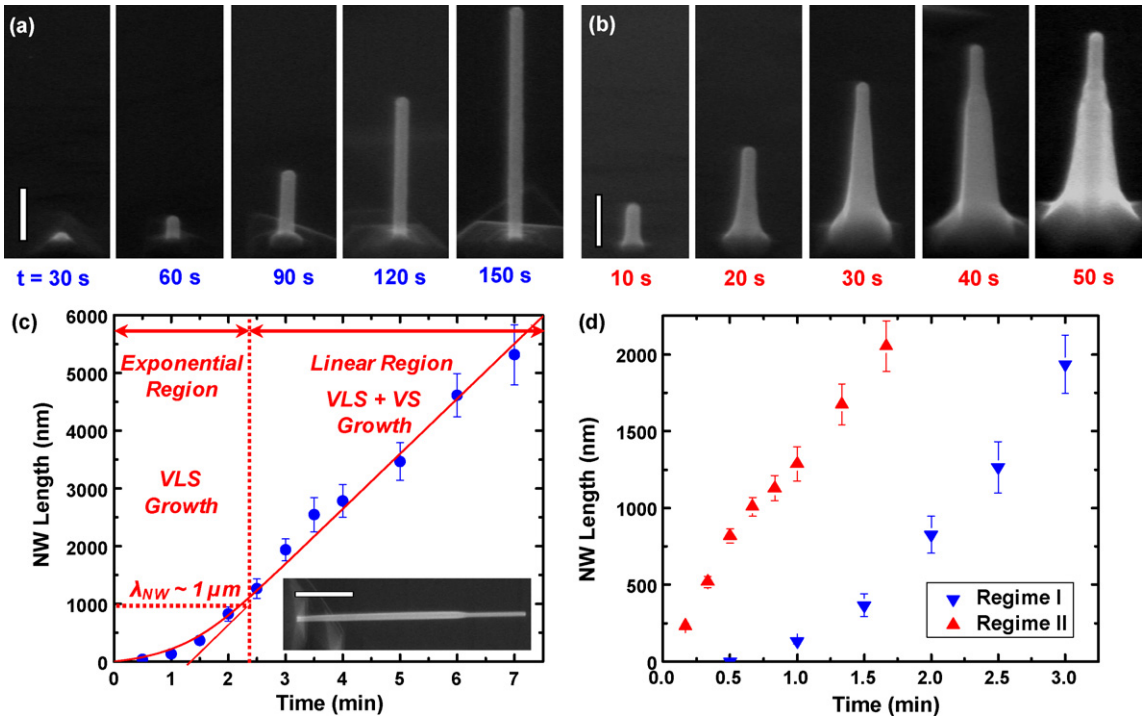

Figure 3 (a) 45° angle view FE-SEM images of InAs NWs grown at a 2.1×10^{-5} TMIn molar fraction at 500 °C. (b) 45° angle view SEM images of InAs NWs grown at a 1.26×10^{-4} TMIn molar fraction and 500 °C. Scale bars are 200 nm. (c) Plot of the NW length as function of time and correspondent growth mode at TMIn molar fraction 2.1×10^{-5}. Inset is a FE-SEM of an InAs NW grown for 7 min. Scale bar is 1.41 μm. (d) Plot of the NW length as function of time showing the exponential and sub-linear growth regimes at 2 different TMIn molar fractions. (Adapted with permission from Ref. [66]. ©2009 American Chemical Society.)

dominant, the NW length increases sub-linearly with time and the NWs are tapered. These experimental results are in excellent agreement with theoretical predictions for NW growth rates as function of time when substrate-NW adatom exchange is taken into account [62]. This also provides the first experimental evidence for reciprocal adatom exchange from the substrate to the NW and identifies growth conditions and lengths over which uniform InAs NW morphology can be attained [61]. This understanding is important to achieve control over radial and axial NW heterostructures employing the InAs material system as demonstrated in Ref. [61].

Independent of the growth substrate, the time-dependent growth rates for GaAs NWs display a distinct behavior from that of InAs NWs. Fig. 4(a) shows FE-SEM images of GaAs NWs grown for different growth times on Si (1 1 1) surfaces at the optimal growth conditions of $T = 417$ °C, from which it is evident that the length of uniform morphology NW increases linearly with growth time. Fig. 4(b) shows plots of the GaAs NW lengths grown on GaAs (1 1 1)B as function of time at different TMGa molar fractions of 7.94×10^{-5} (red triangles, 510 °C) and 6.3×10^{-4} (blue triangles, 410 °C) with 6.5 input V/III ratio. For both TMGa molar fractions, the NW length increases linearly with time, in contrast to the exponential and sub-linear elongation of InAs NWs in the two different growth regimes described earlier. This indicates that adatom exchange between the NW and the growth substrate and hence k_{sub}, as well as sidewall contributions k_{sw} to the total NW growth rate are minimal during the GaAs NW growth. For short growth time, the linear growth rate also indicates adatom incorporation directly at the NW tip since $dl/dt \propto 2\pi r^2$ is independent of l.

The solid-phase diffusion of In adatoms on the NW sidewalls that leads to the non-linear growth rates at short growth times is further supported by the diameter-dependent growth rates for InAs NWs. Fig. 5(a)—(c) shows FE-SEM images of uniform InAs NWs grown for 120 s from 45, 70, and 90 nm Au NP diameters, respectively, patterned by e-beam lithography on the same growth substrate with 2 μm spacing. The growth conditions were similar to those of regime I in Fig. 3(d) — (exponential NW elongation with time), where uniform NW morphology is attained while minimizing the substrate contribution to the growth rate. For GaAs NWs, the diameter-dependent growth rates vary with the growth conditions. Fig. 5(d) shows a plot of the GaAs NW growth rate as a function of diameter at a constant input V/III ratio of 6.5, constant temperature of 440 °C, and for different TMGa molar fractions. The GaAs NW growth rate appears to be independent of the NP diameter in the range of 50—200 nm, and decreases for NPs with diameter <50 nm. This is attributed to the Gibbs—Thomson effect, i.e. the reduction of supersaturation in smaller diameter NPs which leads to lower NW growth rates. However, for a higher input V/III ratio of 54, and for a temperature range of 411—467 °C, the NW growth rate increases sharply for NWs with NP diameter <50 nm. This indicates a switchover from the kinetically limited to the diffusion-limited growth regime which is similar to the diameter dependence of InAs NW growth rates. This switchover may be related to the increase in surface diffusion length upon the NW sidewalls due to surface modi-

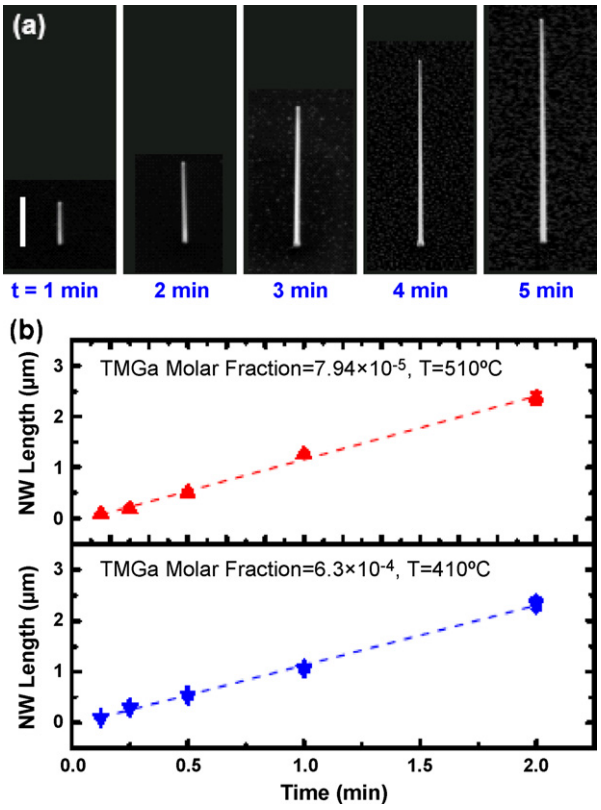

Figure 4 (a) 45° angle view FE-SEM images of GaAs NWs grown on Si (1 1 1) at 5.56×10^{-5} TMGa molar fraction and 1.38×10^{-3} AsH_3 molar fraction at 417 °C at 500 °C. Scale bar is 1 μm. (b) Plot of GaAs NW length as function of time showing linear dependence on GaAs (1 1 1)B surfaces at a TMGa molar fraction of 7.94×10^{-5} (red triangles, 510 °C) and TMGa molar fraction of 6.3×10^{-4} (blue triangles, 410 °C), respectively (V/III = 6.5). (Adapted with permission from Ref. [45]. ©2008 American Chemical Society.)

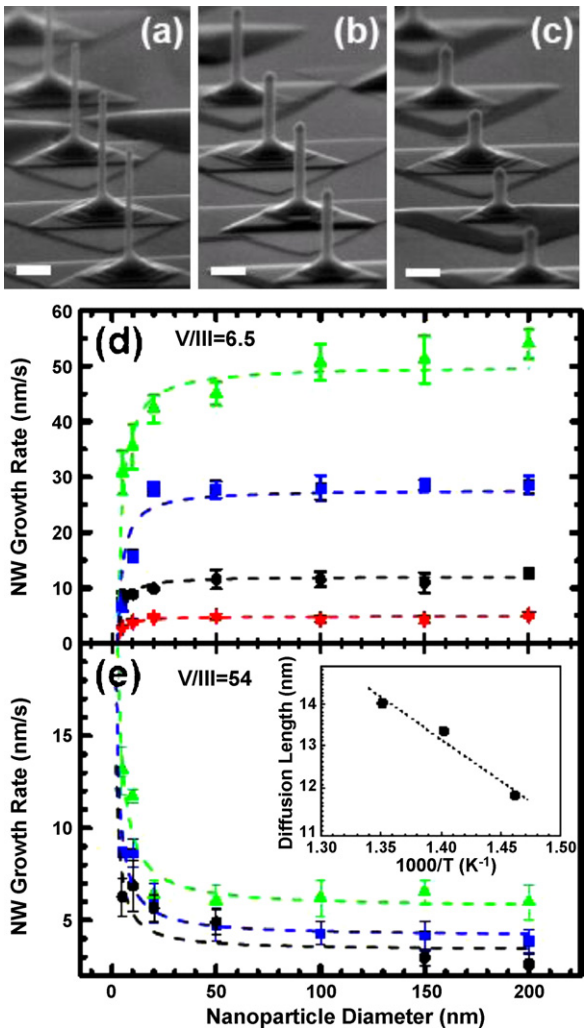

Figure 5 Nanowire growth rate as function of diameter. 45° angle view FE-SEM images of InAs NWs grown at predefined locations on the same substrate for 120 s with different diameters (a) 45 nm, (b) 70 nm, and (c) 90 nm. Scale bars are 200 nm. GaAs NW growth rate vs. Au nanoparticle radius at: (d) V/III = 6.5 and constant growth temperature (Tg = 440 °C) for different TMGa molarfractions of 2.29×10^{-5} (down-triangles), 7.94×10^{-5} (circles), 3.77×10^{-4} (squares) and 6.29×10^{-4} (up-triangles); (e) V/III = 54 and constant TMGa molar fraction of 2.29×10^{-5} for different growth temperatures of Tg = 411 °C (circles), Tg = 440 °C (squares) and Tg = 467 °C (triangles). The inset shows the Arrhenius plot of the extracted diffusion length as a function of temperature. (Adapted with permission from Refs. [45,66]. ©2008 and 2009 American Chemical Society.)

fication at high V/III ratios [45]. If surface diffusion of Ga on the GaAs NWs is taken into account and using Fig. 5(e), one can extract a $\lambda_{NW} \sim 10$ nm for the GaAs NWs [45], a value that is significantly smaller than the one deduced for InAs NWs and reflects the distinct differences in morphology and growth rate dependences observed above.

Crystal structure of InAs and GaAs NWs

Understanding the correlation between the NW crystal structure and transport properties is essential to utilize their full potential for practical applications. Most III—V materials crystallize in the zinc blende crystal structure. However, III—V NWs often show zinc blende (ZB)/wurtzite (WZ) polymorphism under different growth conditions and techniques [63], which has direct consequences on their electronic and optical properties. Indeed, recent studies on rotationally twinned WZ/ZB and pure ZB InP NWs have shown distinct photoluminescence response at low temperatures [64] which was attributed to band-edge discontinuities in the WZ/ZB NWs [65].

Polymorphic WZ/ZB crystal structures have also been observed in our NWs. In the case of InAs NWs, WZ crystal structure was obtained on InAs (1 1 1)B surfaces whereas ZB crystal structure resulted from the growth on SiO_2 surfaces [66]. GaAs NWs grown on both GaAs (1 1 1)B and Si (1 1 1) substrates showed predominantly ZB crystal structure with small WZ segments [46]. The possibility to control the crystal structure by using different growth substrates allowed us to analyze and correlate NW crystallographic and charge transport properties. Fig. 6(a1) and (a2) shows high resolution transmission electron microscope (HR-TEM) images of the same InAs NW grown on InAs (1 1 1)B substrate near its tip, taken at two different pole orientations. This illustrates

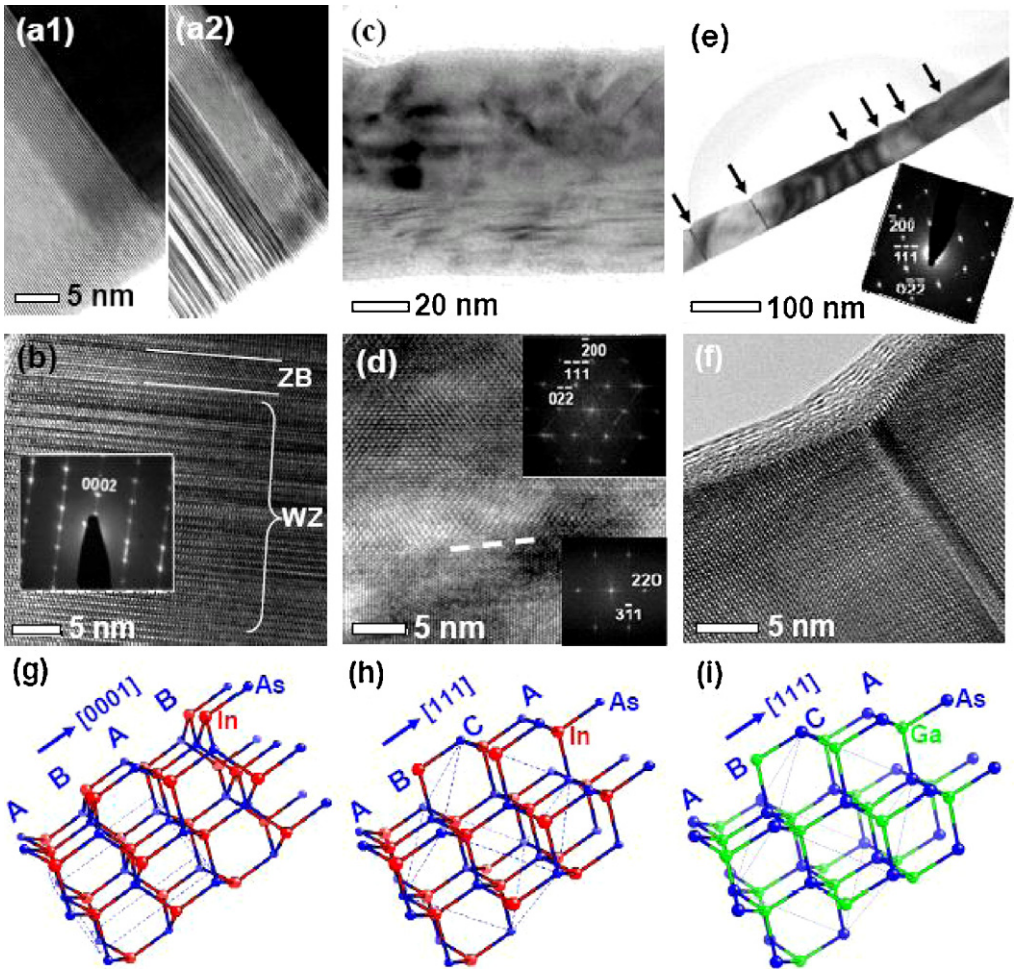

Figure 6 HR-TEM images of an InAs NW grown on InAs (1 1 1)B substrate near its tip taken at a pole orientation of (a1) [0 $\bar{1}$ 1 0] and (a2) [2 $\bar{1}$ $\bar{1}$ 0] where stacking faults are visible. (b) HR-TEM image showing lattice fringes of an InAs NW grown on InAs (1 1 1) B with its correspondent diffraction pattern indicating WZ crystal structure [0 0 0 2] growth orientation. Stacking faults are clearly visible and a small ZB segment is highlighted by 2 white lines. (c) TEM image of an InAs NW grown on SiO_2 substrate. (d) Lattice fringes of same NW in (c) with inset FFT patterns at its top and bottom portions showing ZB crystal structure and [1 1 0] growth orientation for both segments. The dashed line in (d) highlights the interface between the twinned NW segments along the NW axis. (e) TEM image of a GaAs NW with stacking faults marked with dark arrows. Inset is the correspondent diffraction pattern showing ZB crystal structure and [1 1 1] growth orientation. (f) HR-TEM image of a GaAs NW grown on a Si (1 1 1) substrate taken near a stacking fault. (g) Crystal structure for WZ InAs with ABAB layer stacking in the [0 0 0 1] orientation. (h) Crystal structure for ZB InAs with ABCA layer stacking in the [1 1 1] orientation. (i) Crystal structure for ZB GaAs with ABCA layer stacking in the [1 1 1] orientation. (Adapted with permission from references 46 (©2008 American Chemical Society) and 66 (©2009 Wiley-VCH).)

that the stacking faults in the crystal planes perpendicular to the NW axis can only be seen from a certain pole axis of [2 $\bar{1}$ $\bar{1}$ 0] as compared to that of [0 $\bar{1}$ 1 0]. Fig. 6(b) shows a HR-TEM image of an InAs NW grown on InAs (1 1 1)B substrate with its selected area diffraction (SAD) pattern showing WZ crystal structure and [0 0 0 1] growth orientation. Numerous stacking faults and a small ZB segment can also be seen in Fig. 6(b). The stacking fault density did not seem to vary with growth temperature in the range of 450—500 °C or with the V/III ratio of 20—60 [66]. InAs NWs grown on SiO_2/Si substrate (Fig. 6(c)) have exhibited a twinned ZB crystal structure along the NW axis for diameters $\geq$40 nm and [1 1 0] growth orientation as illustrated in Fig. 6(d). This is different to the case of GaAs NWs which, independent of the growth substrate, showed a ZB crystal structure with much lower stacking fault density as illustrated in the TEM image of Fig. 6(e). Fig. 6(f) shows a HR-TEM image of a GaAs NW with its correspondent SAD pattern showing ZB crystal structure and ⟨1 1 1⟩ growth orientation.

For the ZB crystal structure of InAs (Fig. 6(h)) and GaAs (Fig. 6(i)), the layer stacking sequence is the standard ABCABC. Rotation of the third nearest neighbors in the (1 1 1) planes leads to ABAB layer stacking and to the formation of the WZ crystal structure (Fig. 6(g)).

The lattice constants and system energies for ZB and WZ III—V crystals are very similar [67,68] which allows the co-existence of WZ and ZB structures at the same growth conditions. Recently, it has been shown that low supersaturation of indium in the Au nanoparticle favors ZB III—V NWs [69,70]. Consistently with our results on both InAs and

GaAs, low temperature growths seems to yield ZB NW structure [46,71—73], whereas WZ NW structure is favored at higher growth temperatures [74,75]. This has direct impact on the NW electronic properties as discussed in the next section.

Correlation of transport behavior with crystal structure

The capability of bandgap engineering, the direct bandgap, and the high electron mobility of III—V compound semiconductor NWs make them highly interesting for potential electronic and optoelectronic applications. InAs and GaAs NWs have been used to implement a variety of electronic devices including resonant tunneling diodes [76], single electron transistors [77], Josephson junctions [78], light emitting diodes [79], as well as back-gate [80,81], top-gate [72], and surround-gate FETs [82]. From FET measurements, transport coefficients such as carrier mobility and carrier concentration of InAs NWs as function of diameter [83], length [84,85], vertical and lateral fields [86], as well as the effects of surface states on transport and transport coefficient extraction [87] have been determined. On the other hand, transport studies on GaAs NWs are limited by the surface Fermi energy pinning due to acceptor-type states near mid-gap [88] that leads to full depletion of the GaAs NW channels [89]. Here we focus on the correlation between microstructure and transport properties of individual InAs and GaAs NWs.

Fig. 7(a) and (b) shows output characteristics of an InAs NWFET showing ohmic contact behavior and little current modulation of the ZB NW with V_{GS} in Fig. 7(a), in contrast to strong current modulation of the WZ NW with V_{GS} in Fig. 7(b). Fig. 7(c) shows output characteristics obtained from a ZB GaAs NW FET; in this case the current is about three orders of magnitude lower than that achieved with InAs NWs, and very small gate modulation is obtained at comparable bias voltages. The transfer characteristics of these NWs are shown in Fig. 7(d)—(f). ZB InAs

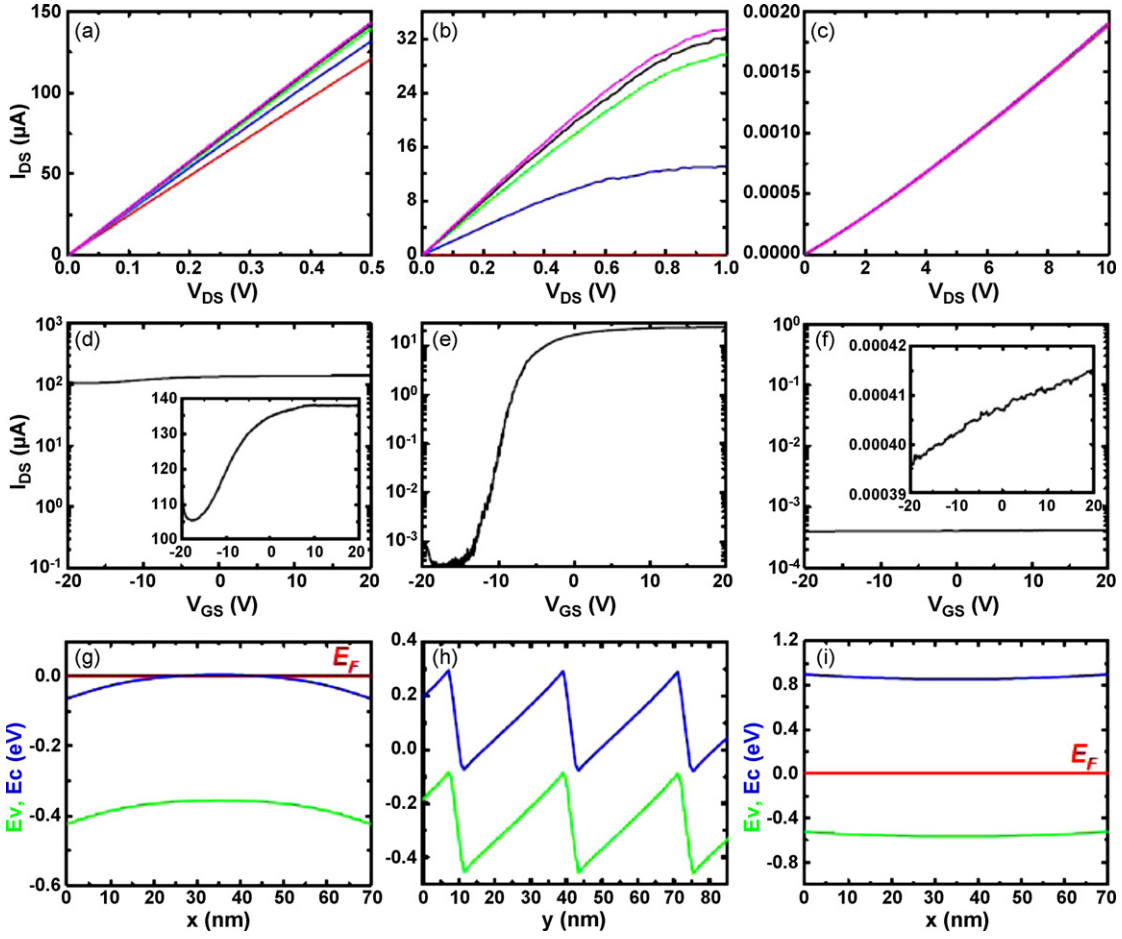

Figure 7 (a)—(c) Output curves of ZB InAs (L_{SD} = 3.4 μm), WZ InAs (L_{SD} = 3.4 μm), and ZB GaAs NWs (L_{SD} = 2 μm), respectively for V_{GS} = −20 to +20 V in 5 V steps. (d)—(f) Transfer curves for the same NWs in (a)—(c) at V_{DS} = 0.5 V for the InAs NWs, and 2.5 V for the GaAs NW. Insets to (d) and (f) are linear scale plots of the correspondent transfer curves. (g) Line cut profile of energy band-edge diagrams across the thickness (x) of a 70 nm InAs slab with $N_D = 5 \times 10^{16}$ cm^{-3} and $Q_s/q = 10^{12}$ cm^{-2} from a Schrödinger—Poisson solver showing strong electron accumulation at the NW surface. (h) Line cut profile of energy band-edges along the channel axis (y) of a WZ NW with ZB segments in the presence of 10^{13} cm^{-2} spontaneous polarization charges. (i) Same as in (g) for an n-type GaAs NW with $N_D = 5 \times 10^{16}$ cm^{-3} and $Q_s/q = -10^{12}$ cm^{-2} showing upward band bending and total depletion of the NW. E_v, E_c, and E_F denote the valence, conduction, and Fermi energy, respectively. (Adapted with permission from Ref. [66]. ©2009 Wiley-VCH).

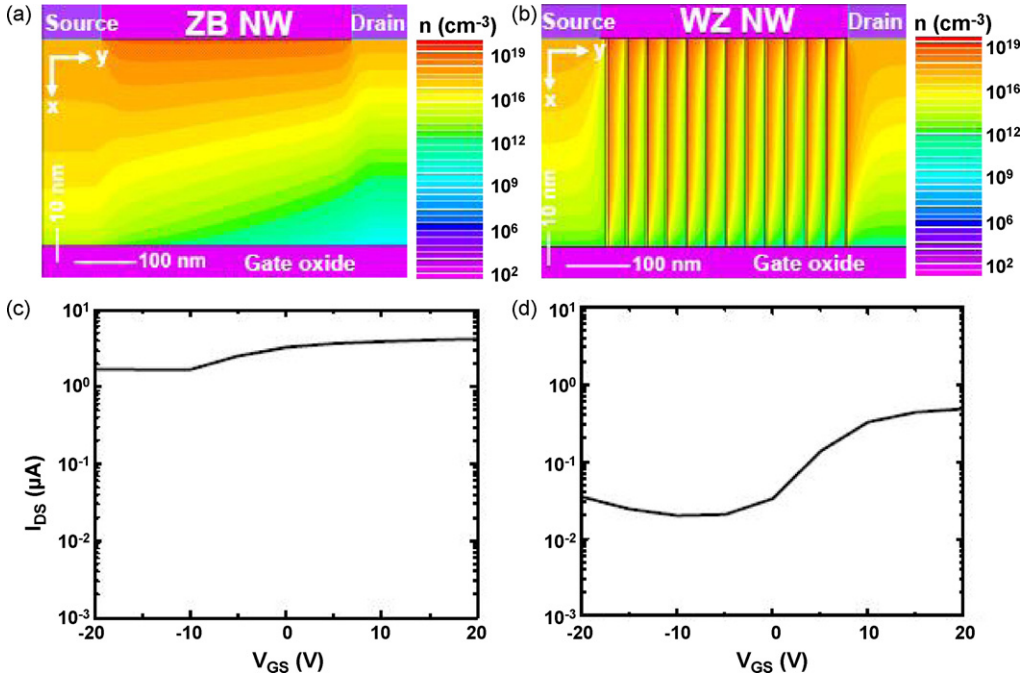

Figure 8 Contour plots from 2D Silvaco simulations of carrier concentration for an InAs slab with (a) pure ZB device and (b) WZ/ZB InAs heterostructure device extracted at $V_{DS} = 0.5$ V and $V_{GS} = -20$ V showing stronger depletion in (b) penetrating deeper across the channel body. Transfer characteristics at $V_{DS} = 0.1$ V for (c) ZB devices and (d) WZ/ZB devices. The trends observed in the output and transfer curves are similar to those measured on the fabricated FETs showing stronger depletion for the WZ devices with ZB segments inserted across the channel length. The current was normalized to a 60 nm × 60 nm slab with $L_{SD} = 400$ nm. (Adapted with permission from Ref. [66]. ©2009 Wiley-VCH).

NWs show an $I_{on}/I_{off} \sim 2$, WZ NWs with ZB segments show $I_{on}/I_{off} \sim 10^4$, and ZB GaAs NWs show virtually no gate effect. The significantly distinct charge transport properties of ZB InAs NWs, WZ InAs NWs and ZB GaAs NWs suggest strong correlation with the different crystal structures discussed above.

Detailed device analysis and extraction of the transport coefficients for WZ and ZB InAs NWs have resulted in little differences that cannot account for the distinct behavior of their subthreshold characteristics [66]. For the ZB InAs NWs, the presence of donor-type surface states pin the Fermi energy in the conduction band leading to electron accumulation at the surface (as illustrated in Fig. 7(g)) and preventing modulation of the free carriers in the channel. This effect is reversed in GaAs NWs where negatively charged acceptor-type surface states [88] lead to full NW depletion as illustrated in the energy band-edge profiles in Fig. 7(i). In these self-consistent simulations of energy band-edge profiles, a typical doping density of $N_D = 5 \times 10^{16}$ cm^{-3} and surface state density of $Q_s/q = 10^{12}$ cm^{-2} was assumed [66]. The case of WZ InAs NWs is distinct: In WZ InAs NWs with small ZB segments the effect of surface states is suppressed due to the lack of inversion symmetry in the WZ crystal structure that leads to the formation of spontaneous polarization charges at the opposite faces of the crystal [90] and enhances depletion near negative polarity charges and accumulation near positive polarity charges. This is indicated by the energy band-edge diagrams in Fig. 7(h).

The effect of spontaneous polarization charges on NW depletion for the WZ InAs NWs with small ZB segments was further investigated by Silvaco-Atlas two-dimensional simulations. Two identical device structures (pure ZB and WZ with ZB segments) with a channel length $L_{SD} = 400$ nm, 60 nm channel thickness and 10^{12} cm^2 surface state density were considered. For the WZ NWs, the 3.5 nm ZB segments were inserted every 28.5 nm based on the HR-TEM image of Fig. 6(d). A spontaneous polarization charge density of 10^{13} cm^{-2}, which is comparable to those of other hexagonal materials [91], was assumed. The piezoelectric (strain-induced) charge density was found to be of the order of $\sim 5 \times 10^{11}$ cm^{-2} and thus have negligible effects on the subthreshold characteristics. Fig. 8(a) and (b) shows contour plots of free carrier concentration for ZB and WZ InAs NWs taken at $V_{GS} = -20$ V and $V_{DS} = 0.5$ V. It can be seen that for the WZ InAs NW, that the depletion extends deep into the channel that will in turn lead to enhanced I_{DS} modulation with V_{GS}. The transfer curves for these 2 devices is shown in Fig. 8(c) and (d), where little modulation is achieved in the ZB InAs NW in the V_{GS} range of −20 to +20 V at $V_{DS} = 0.1$ V whereas modulation of the current by a factor of ∼10 is seen for the WZ InAs NW. The I_{on}/I_{off} ratio here is dominated by short channel effects, which were also seen in our experiment for a device of $L_{SD} \sim 850$ nm with similar I_{on}/I_{off} ratio [66]. The good agreement of the simulation, specifically the NWFET subthreshold characteristics, with the experimental results and simulation further supports our understanding of the strong correlation between electronic transport and structural properties of NWs and could be used to improve NW devices toward practical applications.

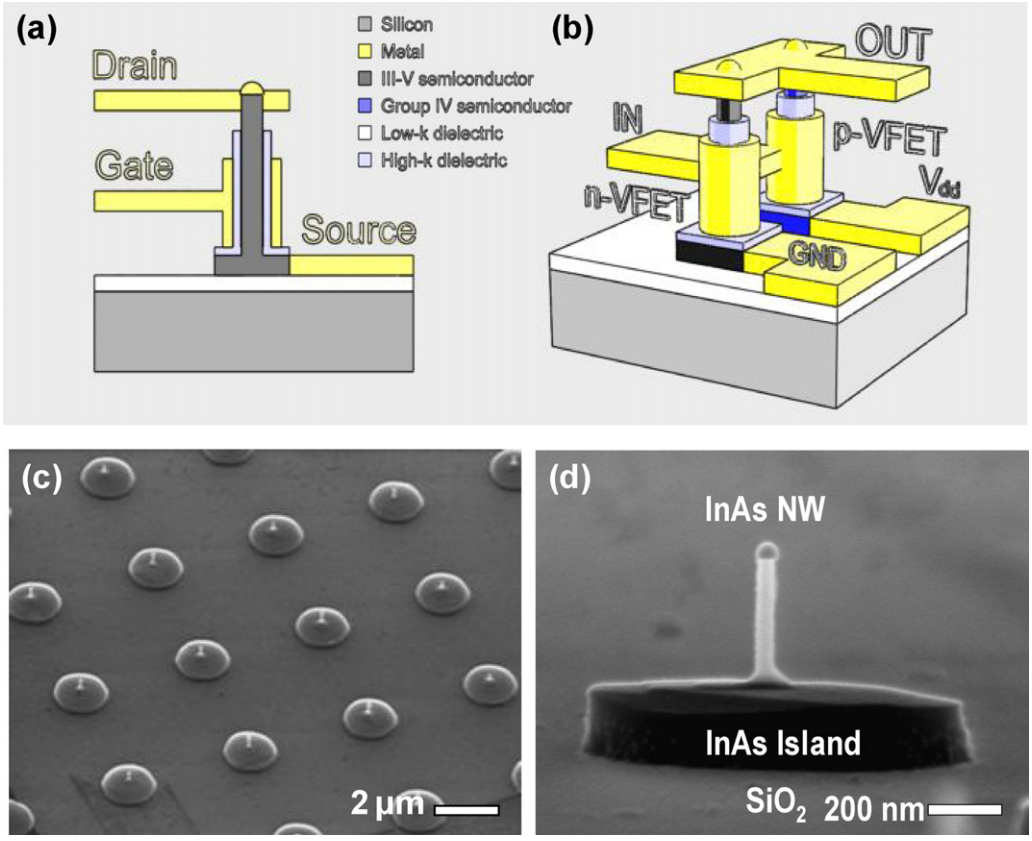

Figure 9 (a) Side-view cartoon of a vertical NWFET on insulator on Si. (b) Cartoon of vertical NWFET integration for complimentary function in an inverter configuration. The presence of the low-*k* dielectric atop Si allows NW isolation for versatile functionality. (c) Realization of vertically integrated and electrically isolated III—V NW arrays on insulator-on-silicon. (d) Cross-sectional FE-SEM image of an InAs NW grown on an InAs island on SiO_2/Si for low resistance ohmic contact at the NW base and electrical isolation. (Reprinted with permission from Ref. [92]. ©2008 American Institute of Physics).

Concluding remarks

The systematic studies on the growth of InAs and GaAs NWs indicate different key physical processes that contribute concomitantly to their growth including kinetically and thermodynamically limited reactions. Although a unified framework for III—V NW growth was identified, the detailed growth conditions for different materials determine the dominant growth regime that results in distinct NW morphology, structure, and transport properties. This understanding of the growth, structure, key transport properties, and their correlation is essential to achieve optimal control over functional NW (opto)electronic devices. Furthermore, the possibility of 3D device architecture designs (Fig. 9) may help enhancing their performance. The capability of III—V NW growth on Si [46] or III—V on insulator on Si enables heterogeneous integration to CMOS technology for hybrid information processing [92].

Specifically for electronic applications, the geometry of the NW permits the realization of surround-gate devices with better control over the channel electrostatics as the FET device dimensions scale further. The vertical surround-gate NWFET devices have been demonstrated by several groups using different materials [14,15,82,93,94]. In order to realize vertical NW circuits and systems, a number of fundamental and technology related issues need to be addressed in time. These include (i) precise control over the NW morphology, crystallinity, and growth direction as well as accurate placement or growth of NWs at specified locations with high yield and reproducibility over large areas, (ii) integration to Si technology mainstream together with electrical isolation and individual addressability (as depicted in Fig. 9(b)) to allow versatile functionality [59], (iii) reduction of parasitic series- and metal contact-resistances at the source and drain regions as well as reduction of parasitic capacitances of contact leads (source/drain/gate) when integrated in 3D, and (iv) overcoming detrimental effects of surface states and improving the high-*k* III—V interface. As some of these issues also evolve in the context of CMOS technology, research on NWs is going to benefit as well as contribute to addressing and overcoming these limitations.

Acknowledgements

We would like to acknowledge the contributions of Prof. Edward T. Yu in the InAs NW studies, Dr. Darija Susac and Prof. Karen L. Kavanagh of Simon Fraser University, Canada for TEM studies, Prof. Paul K.L. Yu for providing access to his OMVPE reactor for InAs NW synthesis, Prof. S.S. Lau, Dr.

Peng Chen, and Yi Jing for smart-cut InAs layer transfer to SiO_2/Si, and David Aplin for help and discussions. Deli Wang is thankful for the generous support of this work by Office of Naval Research, National Science Foundation, Sharp Labs of America, World Class University (WCU) Program at the Sunchon National University (Korea), UCSD Center for Magnetic Recording Research, and UCSD Hellman Fellowship.

References

[1] http://www.itrs.net/Links/2007ITRS/2007_Chapters/2007_ERD.pdf.
[2] R. Chau, S. Datta, M. Doczy, B. Doyle, J. Jin, J. Kavalieros, et al., IEEE Trans. Nanotechnol. 4 (2005) 153.
[3] A.M. Morales, C.M. Lieber, Science 279 (1998) 208.
[4] C. Thelander, P. Agarwal, S. Brongersma, J. Eymery, L.F. Feiner, A. Forchel, et al., Mater. Today 9 (2006) 28.
[5] Y. Li, F. Qian, J. Xiang, C.M. Lieber, Mater. Today 9 (2006) 18.
[6] P.J. Pauzauskie, P. Yang, Mater. Today 9 (2006) 36.
[7] M.S. Gudiksen, C.M. Lieber, J. Am. Chem. Soc. 122 (2000) 8801.
[8] Y.Y. Wu, R. Fan, P.D. Yang, Nano Lett. 2 (2002) 83.
[9] M.T. Bjork, B.J. Ohlsson, T. Sass, A.I. Persson, C. Thelander, M.H. Magnusson, et al., Nano Lett. 2 (2002) 87.
[10] M.S. Gudiksen, L.J. Lauhon, J. Wang, D.C. Smith, C.M. Lieber, Nature 415 (2002) 617.
[11] L.J. Lauhon, M.S. Gudiksen, C.L. Wang, C.M. Lieber, Nature 420 (2002) 57.
[12] M.S. Gudiksen, J.F. Wang, C.M. Lieber, J. Phys. Chem. B 106 (2002) 4036.
[13] J. Tragardh, A.I. Persson, J.B. Wagner, D. Hessman, L. Samuelsson, J. Appl. Phys. 101 (2007) 123701.
[14] H.T. Ng, J. Han, T. Yamada, P. Nguyen, Y.P. Chen, M. Meyyappan, Nano Lett. 4 (2004) 1247.
[15] T. Bryllert, L.E. Wernersson, L.E. Froberg, L. Samuelson, IEEE Electron Dev. Lett. 27 (2006) 323.
[16] F. Qian, S. Gradecak, Y. Li, C.Y. Wen, C.M. Lieber, Nano Lett. 5 (2005) 2287.
[17] C. Soci, A. Zhang, B. Xiang, S.A. Dayeh, D.P.R. Aplin, J. Park, et al., Nano Lett. 7 (2007) 1003.
[18] C. Soci, A. Zhang, X.-Y. Bao, H. Kim, Y. Lo, D. Wang, J. Nanosci. Nanotechnol., in press.
[19] A.B. Greytak, C.J. Barrelet, Y. Li, C.M. Lieber, Appl. Phys. Lett. 87 (2005) 151103.
[20] S.A. Dayeh, C. Soci, P.K.L. Yu, E.T. Yu, D. Wang, J. Vac. Sci. Technol. B 25 (2007) 1432.
[21] X. Jiang, Q. Xiong, S. Nam, F. Qian, Y. Li, C.M. Lieber, Nano Lett. 7 (2007) 3214.
[22] S. Gradecak, F. Qian, Y. Li, H.G. Park, C.M. Lieber, Appl. Phys. Lett. 87 (2005) 173111.
[23] R.S. Wagner, W.C. Ellis, Appl. Phys. Lett. 4 (1964) 89.
[24] A.I. Persson, M.W. Larsson, S. Stenstrom, B.J. Ohlsson, L. Samuelson, L.R. Wallenberg, Nat. Mater. 3 (2004) 677.
[25] L.C. Campos, M. Tonezzer, A.S. Ferlauto, V. Grillo, R. Magalhaes-Paniago, S. Oliveira, et al., Adv. Mater. 20 (2008) 1499.
[26] Z.L. Wang, J. Phys. Condens. Matter 16 (2004) R829.
[27] W.S. Shi, Y.F. Zheng, N. Wang, C.S. Lee, S.T. Lee, Appl. Phys. Lett. 78 (2001) 3304.
[28] T.J. Trentler, K.M. Hickman, S.C. Goel, A.M. Viano, P.C. Gibbons, W.E. Buhro, Science 270 (1995) 1791.
[29] M.J. Bierman, Y.K.A. Lau, A.V. Kvit, A.L. Schmitt, S. Jin, Science 320 (2008) 1060.
[30] J. Zhu, H.L. Peng, A.F. Marshall, D.M. Barnett, W.D. Nix, Y. Cui, Nat. Nanotechnol. 3 (2008) 477.
[31] K. Haraguchi, T. Katsuyama, K. Hiruma, K. Ogawa, Appl. Phys. Lett. 60 (1992) 745.
[32] L.E. Jensen, M.T. Bjork, S. Jeppesen, A.I. Persson, B.J. Ohlsson, L. Samuelson, Nano Lett. 4 (2004) 1961.
[33] J.C. Harmand, G. Patriarche, N. Pere-Laperne, M.N. Merat-Combes, L. Travers, F. Glas, Appl. Phys. Lett. 87 (2005) 203101.
[34] H.D. Park, S.M. Prokes, R.C. Cammarata, Appl. Phys. Lett. 87 (2005) 063110.
[35] X.F. Duan, C.M. Lieber, J. Am. Chem. Soc. 122 (2000) 188.
[36] F. Wang, A. Dong, J. Sun, R. Tang, H. Yu, W.E. Buhro, Inorg. Chem. 45 (2006) 7511.
[37] R.S. Wagner, W.C. Ellis, Trans. Metall. Soc. AIME 233 (1965) 1053.
[38] E.I. Givargizov, Highly Anisotropic Crystals, Terra Scientific Pub. Co., Tokyo, Japan, 1987.
[39] G.A. Bootsma, H.J. Gassen, J. Cryst. Growth 10 (1971) 223.
[40] E.I. Givargizov, Kristall und Technik 10 (1975) 473.
[41] S.A. Dayeh, E.T. Yu, D. Wang, Nano Lett. 7 (2007) 2486.
[42] K.A. Dick, K. Deppert, T. Martensson, B. Mandl, L. Samuelson, W. Seifert, Nano Lett. 5 (2005) 761.
[43] S.A. Dayeh, E.T. Yu, D. Wang, Small 3 (2007) 1683.
[44] S.A. Dayeh, E.T. Yu, D. Wang, J. Phys. Chem. C 111 (2007) 13331.
[45] C. Soci, X.-Y. Bao, D.P.R. Aplin, D. Wang, Nano Lett. 8 (2008) 4275.
[46] X.Y. Bao, C. Soci, D. Susac, J. Bratvold, D.P.R. Aplin, W. Wei, et al., Nano Lett. 8 (2008) 3755.
[47] K.A. Dick, K. Deppert, L.S. Karlsson, L.R. Wallenberg, L. Samuelson, W. Seifert, Adv. Funct. Mater. 15 (2005) 1603.
[48] D.H. Reep, S.K. Ghandhi, J. Electrochem. Soc. 131 (1984) 2697.
[49] O. Mizuno, H. Watanabe, D. Shinoda, Jpn. J. Appl. Phys. 14 (1975) 184.
[50] C.A. Larsen, S.H. Li, N.I. Buchan, G.B. Stringfellow, D.W. Brown, J. Cryst. Growth 102 (1990) 126.
[51] P. Paiano, P. Prete, N. Lovergine, A.M. Mancini, J. Appl. Phys. 100 (2006).
[52] D.H. Reep, S.K. Ghandhi, J. Electrochem. Soc. 130 (1983) 675.
[53] W. Seifert, M. Borgstrom, K. Deppert, K.A. Dick, J. Johansson, M.W. Larsson, et al., J. Cryst. Growth 272 (2004) 211.
[54] M.T. Borgstrom, G. Immink, B. Ketelaars, R. Algra, E. Bakkers, Nat. Nanotechnol. 2 (2007) 541.
[55] J. Bauer, V. Gottschalch, H. Paetzelt, G. Wagner, B. Fuhrmann, H.S. Leipner, J. Cryst. Growth 298 (2007) 625.
[56] J. Johansson, C.P.T. Svensson, T. Martensson, L. Samuelson, W. Seifert, J. Phys. Chem. B 109 (2005) 13567.
[57] V.G. Dubrovskii, N.V. Sibirev, R.A. Suris, G.E. Cirlin, V.M. Ustinov, M. Tchernysheva, et al., Semiconductors 40 (2006) 1075.
[58] Z. Chen, C. Cao, Appl. Phys. Lett. 88 (2006) 143118.
[59] S.A. Dayeh, D. Susac, C. Peng, J. Yi, K.L. Kavanagh, S.S. Lau, et al., Optimal control over the InAs nanowire growth for system integration and their structural and transport properties, in: 8th IEEE Conference on Nanotechnology, Arlington, TX, USA, 2008, p. 576.
[60] I. Avramov, Nanoscale Res. Lett. 2 (2007) 235.
[61] S.A. Dayeh, E.T. Yu, D.L. Wang, Nano Lett. 9 (2009) 1967.
[62] V. Ruth, J.P. Hirth, J. Chem. Phys. 41 (1964) 3139.
[63] K. Takahashi, T. Moriizumi, Jpn. J. Appl. Phys. 5 (1966) 657.
[64] J. Bao, D.C. Bell, F. Capasso, J.B. Wagner, T. Mårtensson, J. Trägårdh, et al., Nano Lett. 8 (2008) 836.
[65] M. Murayama, T. Nakayama, Phys. Rev. B 49 (1994) 4710.
[66] S.A. Dayeh, D. Susac, K.L. Kavanagh, E.T. Yu, D. Wang, Adv. Funct. Mater., in press, http://dx.doi.org/10.1002/adfm.200801307.
[67] T. Akiyama, K. Sano, K. Nakamura, T. Ito, Jpn. J. Appl. Phys. 45 (2006) L275.
[68] Z. Zanolli, F. Fuchs, J. Furthmuller, U.V. Barth, F. Bechstedt, Phys. Rev. B (Condens. Matter Mater. Phys.) 75 (2007) 245121.
[69] R.E. Algra, M.A. Verheijen, M.T. Borgstrom, L.F. Feiner, G. Immink, W.J.P. van Enckevort, et al., Nature 456 (2008) 369.

[70] P. Caroff, K.A. Dick, J. Johansson, M.E. Messing, K. Deppert, L. Samuelson, Nat. Nanotechnol. 4 (2009) 50.
[71] M. Koguchi, H. Kakibayashi, M. Yazawa, K. Hiruma, T. Katsuyama, Jpn. J. Appl. Phys. Part 1: Regul. Pap. Short Notes Rev. Pap. 31 (1992) 2061.
[72] S.A. Dayeh, D.P.R. Aplin, X.T. Zhou, P.K.L. Yu, E.T. Yu, D.L. Wang, Small 3 (2007) 326.
[73] Q. Hang, F. Wang, P.D. Carpenter, D. Zemlyanov, D. Zakharov, E.A. Stach, et al., Nano Lett. 8 (2008) 49.
[74] K. Hiruma, M. Yazawa, T. Katsuyama, K. Ogawa, K. Haraguchi, M. Koguchi, et al., J. Appl. Phys. 77 (1995) 447.
[75] M.T. Bjork, A. Fuhrer, A.E. Hansen, M.W. Larsson, L.E. Froberg, L. Samuelson, Phys. Rev. B (Condens. Matter Mater. Phys.) 72 (2005) 201307.
[76] M.T. Bjork, B.J. Ohlsson, C. Thelander, A.I. Persson, K. Deppert, L.R. Wallenberg, et al., Appl. Phys. Lett. 81 (2002) 4458.
[77] C. Thelander, T. Martensson, M.T. Bjork, B.J. Ohlsson, M.W. Larsson, L.R. Wallenberg, et al., Appl. Phys. Lett. 83 (2003) 2052.
[78] Y.-J. Doh, J.A. van Dam, A.L. Roest, E.P.A.M. Bakkers, L.P. Kouwenhoven, S. De Franceschi, Science 309 (2005) 272.
[79] K. Hiruma, K. Haraguchi, M. Yazawa, Y. Madokoro, T. Katsuyama, Nanotechnology 17 (2006) S369.
[80] Q.T. Do, K. Blekker, I. Regolin, W. Prost, F.J. Tegude, IEEE Electron Dev. Lett. 28 (2007) 682.
[81] M. Piccin, G. Bais, V. Grillo, F. Jabeen, S. De Franceschi, E. Carlino, et al., Physica E 37 (2007) 134.
[82] C. Thelander, L.E. Froberg, C. Rehnstedt, L. Samuelson, L.E. Wemersson, IEEE Electron Dev. Lett. 29 (2008) 206.
[83] S.A. Dayeh, E.T. Yu, D.L. Wang, Small 5 (2009) 77.
[84] X. Zhou, S.A. Dayeh, D. Aplin, D. Wang, E.T. Yu, Appl. Phys. Lett. 89 (2006) 053113.
[85] X. Zhou, S.A. Dayeh, D. Aplin, D. Wang, E.T. Yu, J. Vac. Sci. Technol. B 24 (2006) 2036.
[86] S.A. Dayeh, D. Susac, K.L. Kavanagh, E.T. Yu, D. Wang, Nano Lett. 8 (2008) 3114.
[87] S.A. Dayeh, C. Soci, P.K.L. Yu, E.T. Yu, W. Deli, Appl. Phys. Lett. 90 (2007) 162112.
[88] W.E. Spicer, I. Lindau, P. Skeath, C.Y. Su, J. Vac. Sci. Technol. 17 (1980) 1019.
[89] A.D. Schricker, F.M. Davidson, R.J. Wiacek, B.A. Korgel, Nanotechnology 17 (2006) 2681.
[90] H. Morkoç, Nitride Semiconductors and Devices, Springer—Verlag, Berlin, 1999.
[91] F. Bernardini, V. Fiorentini, D. Vanderbilt, Phys. Rev. B 56 (1997) R10024.
[92] S.A. Dayeh, C. Peng, Y. Jing, E.T. Yu, S.S. Lau, D. Wang, Appl. Phys. Lett. 93 (2008) 203109.
[93] J. Goldberger, A.I. Hochbaum, R. Fan, P.D. Yang, Nano Lett. 6 (2006) 973.
[94] V. Schmidt, H. Riel, S. Senz, S. Karg, W. Riess, U. Gosele, Small 2 (2006) 85.

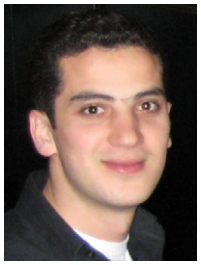

Shadi A. Dayeh is a Director's Postdoctoral Fellow at the Center of Integrated Nanotechnologies, Los Alamos National Laboratories. He obtained a Maitrise-en-Sciences in Physics/Electronics from the Lebanese University, Beirut, Lebanon in 2001, a M.S. degree in Electrical Engineering from Southern Methodist University, Dallas, Texas in 2003, and his Ph.D. degree in Electrical Engineering (Applied Physics) from the University of California, San Diego in 2008. His research concerns with the growth, characterization, and integration of III—V and Si/Ge semiconductor nanowires.

Cesare Soci received his Laurea (M.S. equivalent) and his Ph.D. in Physics from the University of Pavia in 2001 and 2005, respectively. He was a postdoctoral researcher at the Center for Polymers and Organic Solids at the University of California - Santa Barbara in 2005—2006. In 2006 he joined the Electrical and Computer Engineering department at the University of California - San Diego where he is continuing his postdoctoral research. He will become an assistant professor at the Nanyang Technological University in 2009.

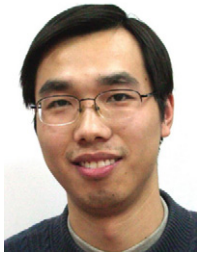

Xinyu Bao received his B.S. in Physics from the University of Science and Technology of China in 2001, and the Ph.D. in Physics from the Institute of Physics, Chinese Academy of Sciences in 2006. He was a postdoctoral researcher at University of California San Diego, working on III—V nanowire growth and characterization from 2006 to 2008. He is currently with the Department of Electrical Engineering at Stanford University working on high efficiency solar cells.

Deli Wang received his B.S. degree in 1990 from the University of Science and Technology of China in Material Sciences and Engineering. From 1990 to 1996, he worked in Changchun Institute of Applied Chemistry, Chinese Academy of Sciences. He earned his Ph.D. in 2001 in the Materials Department of the University of California at Santa Barbara. He then worked as a postdoctoral fellow at Harvard University. He joined the University of California - San Diego in 2004 as an assistant professor at the Electrical and Computer Engineering department. His research interests include rational synthesis of semiconductor nanowires and the application in electronics, optoelectronics, renewable energy, and biosensing and medicines.